Supplementary Material

I. BRIEF REMINDER OF THE HARPER-HOFSTADTER BAND STRUCTURE: EDGE STATES AND CHERN NUMBERS

In this work, we illustrate the cold-atom elevator scheme using the paradigmatic Harper-Hofstadter (HH) model, which describes hopping of particles on a two-dimensional square lattice with a homogenous magnetic flux ϕ per plaquette. The HH Hamiltonian can be written in the Landau gauge as

$$\hat{H} = -J \sum_{m,n} \left(e^{-i\phi n} \hat{a}^\dagger_{m+1,n} \hat{a}_{m,n} + \hat{a}^\dagger_{m,n+1} \hat{a}_{m,n} + \text{h.c.} \right), \tag{S1}$$

where the operators $\hat{a}_{m,n}$ ($\hat{a}^\dagger_{m,n}$) annihilate (create) a particle on the lattice site $\ell = (m,n)$, where m and n denote the site indices along the x and y directions, respectively. The uniform flux per plaquette $\phi = 2\pi\alpha$ is defined modulo 2π. For a rational flux $\alpha = p/q$, with (p,q) prime numbers, the single-particle spectrum splits into q subbands. When represented as a function of the flux α, these energy bands form a fractal structure known as the Hofstadter butterfly.

The finite (uniform) flux per plaquette ϕ breaks time-reversal symmetry, hence leading to non-trivial topological properties: the Hofstadter bands are associated with a non-zero (first) Chern number. Considering the flux $\alpha = 1/4$ as an example, the HH model exhibits 4 subbands, with the middle two bands touching at singular (Dirac) points [Fig. S1(a)]. The lowest and the highest bands share the same Chern number $C = 1$; while the middle degenerate band is associated with the Chern number $C = -2$.

Under open boundary conditions, the model hosts chiral edge modes whose energies are located within the bulk energy gaps; these edge states can be identified in the red spectrum displayed in Fig. S1(b), where a steeper slope reflects the low density of (edge) states within the bulk gaps. Considering the flux $\alpha = 1/4$ (main text), the two bulk gaps each hosts a single edge mode. The chirality of these two edge modes are opposite: the edge mode located in the lowest (resp. highest) bulk gap propagates in a clockwise (resp. anti-clockwise) manner; see also Fig. 2(d) and (f) in the main text, where these two opposite chiral motions are revealed using the elevator scheme.
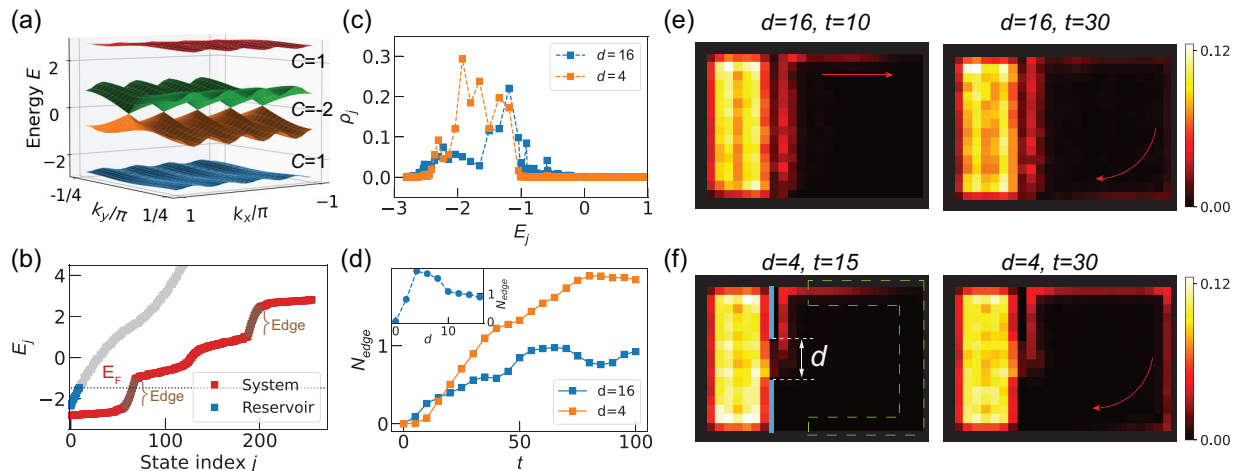

FIG. S1. **Edge state injection with a trivial reservoir.** (a) Energy spectrum as a function of quasimomenta k_x and k_y. We set the lattice constant $a = 1$. The Chern numbers of the separated bands are $C = 1, -2, 1$, respectively. (b) Energy spectrum as a function of the state indices. The blue and red dots correspond to the Hamiltonian describing the trivial reservoir (with chemical potential $\epsilon_R = 1.5$) and the Hofstadter system, respectively. We consider a trivial reservoir of size 7×16 which is coupled to a system of size 16×16 with flux $\phi = \pi/2$ per plaquette. A high wall (one site wide) is placed between the reservoir and the system [blue lines in (f)], which leaves a door of width d open in the middle. (c) Population of HH eigenstates ρ_j as a function of their energy E_j for different door width d, at time $t = 40$. (d) Number of the injected particles in the edge as a function of the time for different door width d. Inset: The number of particles in the edge as a function of d at $t = 100$. Snapshots of spatial density distribution for (e) $d = 16$, (f) $d = 4$. The green dashed line indicates the region used to count the number of particles at the edge, and the blue bonds represent the high wall. Initially there are $N = 10$ particles in the reservoir, and the on-site potential in the reservoir is suddenly lifted to the value $\epsilon_R = 1.5$. Energy and time are in units of J and $\hbar/J$, respectively. The arrows in (e) and (f) are a guide to the eye for the chiral motion.

II. EDGE-STATE INJECTION

A. Using a trivial reservoir

In the main text, we have shown that chiral edge states can be populated in an energy-selective manner, using a system-reservoir setting immersed in a uniform magnetic flux. In this Appendix, we show that a trivial reservoir (i.e. a reservoir without flux) can also be used to inject particles into the edge states of a quantum Hall system.

Similarly to the sketch in Fig. 1(a) in the main text, we couple a system described by the HH model to a reservoir without magnetic flux. Initially, the reservoir is filled with free fermions, and the system is empty. Suddenly lifting the reservoir on-site potential ϵ_R, such that the energy of the particles in the reservoir becomes resonant with an edge mode of the system [Fig. S1(b)], is found to generate chiral edge currents in the system [Fig. S1(e)]. Even though only a small fraction of particles are injected into the edge states in this case, we find that applying a high wall between the reservoir and the system [see blue bonds in Fig. S1(f)], but leaving a small door open in the middle of the wall, can improve the efficiency. In Fig. S1(f), we plot the snapshots of density distributions of the time-evolved state using a small door opening of width $d = 4$, from which we observe stronger chiral edge currents appearing in the system. We attribute the better efficiency of the door-opening configuration to the fact that a wider range of quasi-momenta is offered by a smaller door width, thus allowing for the population of more edge states in the system; see Fig. S1(c) where we plot the population of HH eigenstates for different d.

By monitoring the number of particles N_{edge} injected in a specific region of the edge [depicted by the dashed lines in Fig. S1(f)], we find that tuning the door width d manifests as a way of controlling the number of particles injected into the edge states, as shown in Fig. S1(d). In the inset of (d), we plot N_{edge} as a function of the door width d at time $t = 100$, and the optimal fraction of injected particles is found at a door width of intermediate size.

B. Spectroscopy resolution

In the main text, we show that our edge-state injection scheme can be used as a spectroscopic probe of the lattice band structure. The resolution of this probe will depend on the band-width of the reservoir (as set by the tunneling amplitude J_R), and on the system-reservoir coupling strength (which we generally set to $J_{RS} = J_R$ in our calculations). To further analyze this resolution aspect, we now study the population of the system's eigenstates as one varies the system-reservoir coupling J_{RS} (while keeping $J_R = 1$ fixed inside the reservoir); see Fig. S2 displayed below. These results illustrate how using a weaker coupling (e.g. $J_{RS} = 0.4$) indeed allows for a better resolution of the populated edge states. Besides, we note that resolving the edge-state branch in the system requires that the reservoir's bandwidth should be smaller than the target band-gap in the system (where the edge-state branch is located). In case the reservoir's tunneling amplitude J_R cannot be reduced to a small value $J_R \ll J$, one can still obtain a satisfactory energy-resolution of the populated edge states by lowering the filling of the reservoir (i.e. by only filling low-energy eigenstates in the reservoir; see e.g. Fig. S1).
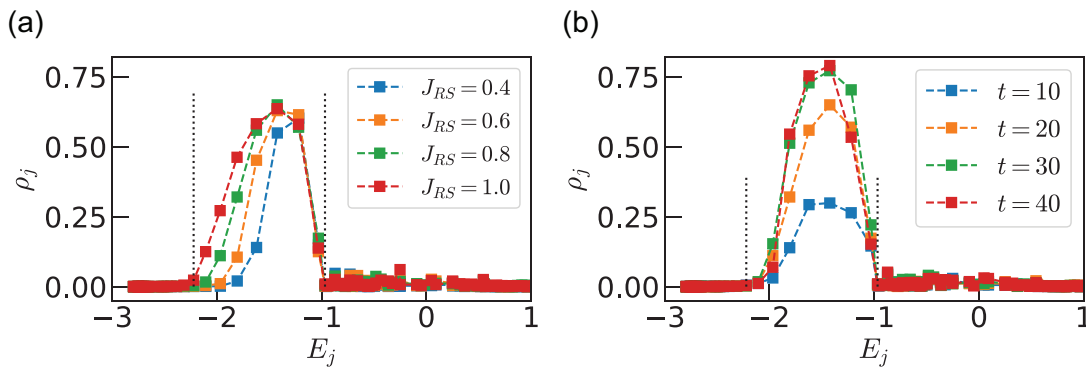

FIG. S2. (a) Population of HH eigenstates ρ_j as a function of their energy E_j for different strength of coupling between system and reservoir J_{RS} at time $t = 20$; here we fix $J_R = 1$ inside the reservoir. (b) Population of HH eigenstates ρ_j as a function of E_j for different observation time t at $J_{RS} = 0.8$. Here, we consider $N = 19$ particles in a reservoir of size 7×12 coupled to a system of size 13×12 and with flux $\phi = \pi/2$ per plaquette.

C. From sharp to smooth box traps

Box traps are an important tool for reaching ultra-low entropies in quantum gas microscopes, which requires fine control of the energy landscape [1]. In order to provide more quantitative numbers, state-of-the-art experiments are able to control the flatness of the potential down to a level that is on the order of a few tens of Hz, which is typically about two orders of magnitude lower than the Hubbard on-site interaction energy. This underlines the feasibility of our proposed scheme. In terms of spatial resolution, high-numerical-aperture imaging systems enable addressing on the order of 500nm, hence allowing for single-site addressability as recently demonstrated for a short-spacing lattice with a lattice constant of 383.5nm [99], or as demonstrated in the context of many-body localization [100].

In the main text, we have considered ideal box-type potentials (infinitely abrupt walls) to illustrate the principle of our proposed method. We have systematically checked that our results do not qualitatively change as one smoothens the box potentials (e.g. by considering a convolution of the box-trap potentials by a Gaussian). Here, we show how the dynamics are modified as one smoothens the box traps, based on the edge-state-injection scheme; see Fig. S3 displayed below. While smoothening the box potential leads to a reduction of the edge-mode velocity (in agreement with previous studies, e.g. [58]), our results convincingly show that the injection of particles from the reservoir into the system (and hence, the activation of the edge current, in this example) does not rely on having perfectly abrupt box potentials in our elevator scheme.

In addition to shaping the potential energy landscape, our scheme requires that the relative energy between the reservoir and the systems should be controlled. This can either be achieved with a digital micromirror device (DMD), which allows for refresh rates that are large compared to the typical time scales in cold-atom experiments, or by using two independent light sources, such that the potential of the reservoir can simply be adjusted by changing the intensity of one of the two laser sources.
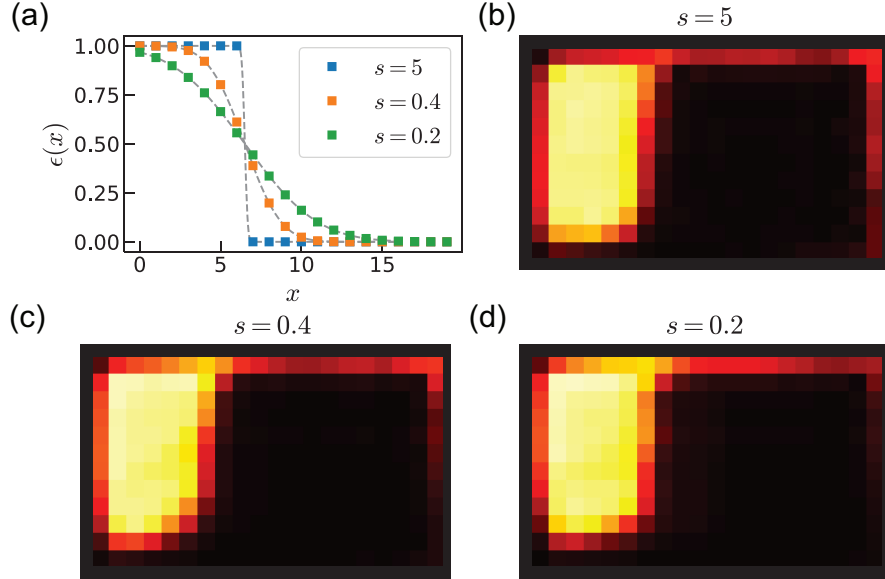

FIG. S3. (a) On-site potentials $\epsilon(x)$ as a function of the horizontal lattice indices x. Motivated by the Munich experiment [43], we use an error function to describe the sharpness of the boundary between the system and the reservoir. Namely, the on-site potentials for each row takes the following form, $\epsilon(x) = \frac{\epsilon_R}{\sqrt{\pi}} \int_0^{-s(x-x_0-1/2)} e^{-t^2} dt + \frac{\epsilon_R}{2}$, where the parameter s determines the sharpness. Dashed lines are a guide to the eye. Snapshots of spatial density distribution at time $t = 20$ for (b) $s = 5$, (c) $s = 0.4$ and (d) $s = 0.2$.

III. CHERN INSULATOR PREPARATION USING THE INJECTION SCHEME

Here, we investigate the possibility of preparing a CI based on injecting particles from a reservoir into an empty system. As an example, we partition a large box of size 12×12 into a sub-box of size 8×8 at the center (the "system") and we define the rest as a trivial reservoir (without magnetic flux). The middle sub-box is our target system, described by the HH model with flux $\phi = \pi/2$ per plaquette. We first analyze the ground-state properties

of such a system-reservoir setup. Figure S4(c) shows the bulk density n_B as a function of the reservoir potential ϵ_R. The incompressible nature of the CI ground state manifests as a plateau in the bulk density. Its topological nature can be confirmed from the local Středa's marker shown by the red dots in Fig. S4(c), which forms a plateau around 1 in the region with bulk density saturation, which is in agreement with the Chern number $C = 1$ of the occupied lowest band.
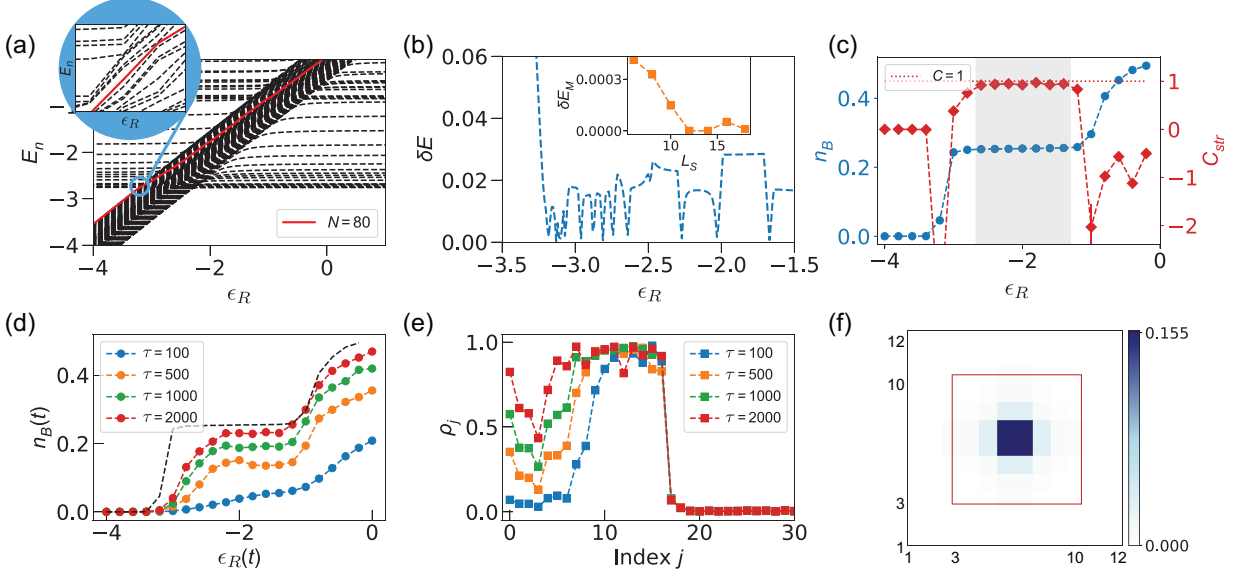

FIG. S4. **Preparing a Chern insulator based on injection.** (a) Energy spectra of the entire setup as a function of ϵ_R. The red line indicates the Fermi level. Considering a box of size 12×12 with a target system being a 8×8 sub-box at the center, the Fermi level corresponds to the 80th eigenvalue. (b) Energy gap (difference between the 80th and 81st eigenvalues) for $J_R = 0.15$. The minimal energy splitting is found to be $\delta E_M = 0.00033$. Inset: the minimal energy splitting δE_M as a function of the system length L_{sys}; here, we consider square boxes of increasing size $L \times L$, and keep the ratio $L/L_{\mathrm{sys}} \simeq 1.6$ constant. (c) The bulk density and the local Středa marker as a function of ϵ_R. The bulk density is evaluated within the central 4×4 sites. The shadow indicates the regime of Chern insulator ground states in the system. (d) The bulk density as a function of ϵ_R for different τ. The black dashed line is the ground state density shown in (c), which represents the adiabatic limit. Here we linearly ramp up ϵ_R from -4 until 0 within time τ, with the initial state being a fully filled trivial reservoir. (e) The population of the eigenstates of the Hofstadter model. We ramp up ϵ_R from -4 until -1.76 by using a saturation function with time τ. (f) The spatial density distribution of a typical isolated bulk state with index $j = 3$.

Based on this ground-state property, one can envisage to adiabatically prepare a CI by slowly ramping up the reservoir potential ϵ_R. In our setup, such an adiabatic limit will be determined by the energy gap δE just above the Fermi level. A typical avoided-crossing is shown in the inset of Fig. S4(a), and the energy gap δE as a function of ϵ_R is plotted in Fig. S4(b). We find that, in order to build up a CI by ramping up ϵ_R, one has to pass through an energy gap as small as $\delta E_M = 0.00033$, which complicates the preparation in practice. The bulk density is plotted in Fig. S4(d) for different ramping times τ, upon using a linear ramping up of ϵ_R. It shows that thousands of tunneling times ($\sim 1/\delta E$) would be required to approach the adiabatic limit for this system size; see also the scaling shown in the inset of Fig. S4(b).

As regards the preparation of a large CI through particle injection, another difficulty concerns the presence of isolated eigenstates deep in the bulk of the system. Considering an improved ramp (based on a saturation function), we obtain the eigenstate populations ρ_j displayed in Fig. S4(e). Here we identify some dips in the eigenstate populations: those dips correspond to eigenstates that are located deep in the bulk, and which are essentially isolated from the reservoir. The spatial density distribution of such a typical isolated eigenstate is shown in Fig. S4(f), with the red box indicating the boundary between the target system and the reservoir.

The existence of eigenstates located deep in the bulk, which are essentially decoupled from the reservoir, complicate the perfect filling of the target topological band. This issue can be solved by improving the system-reservoir coupling (e.g. by increasing the system-reservoir interface or considering a double-layer configuration), or by considering systems with (strong) interactions; see main text and Section IV below.

IV. FRACTIONAL CHERN INSULATOR PREPARATION USING THE INJECTION SCHEME

A. Using a linear ramp

Despite the difficulties mentioned above, injecting particles into an empty system can still be used to prepare a strongly-correlated FCI state, as demonstrated in Fig. 3 in the main text. The reasons are twofold. First, considering a small FCI droplet, the many-body gap across the injection process can potentially remain (reasonably) large due to finite size effects. Second, the strong interactions potentially prevent the isolation of bulk states, as previously illustrated in Figs. S4(e)-(f). As a further demonstration, here we show that a linear ramp of ϵ_R can also be used to prepare a small FCI droplet.
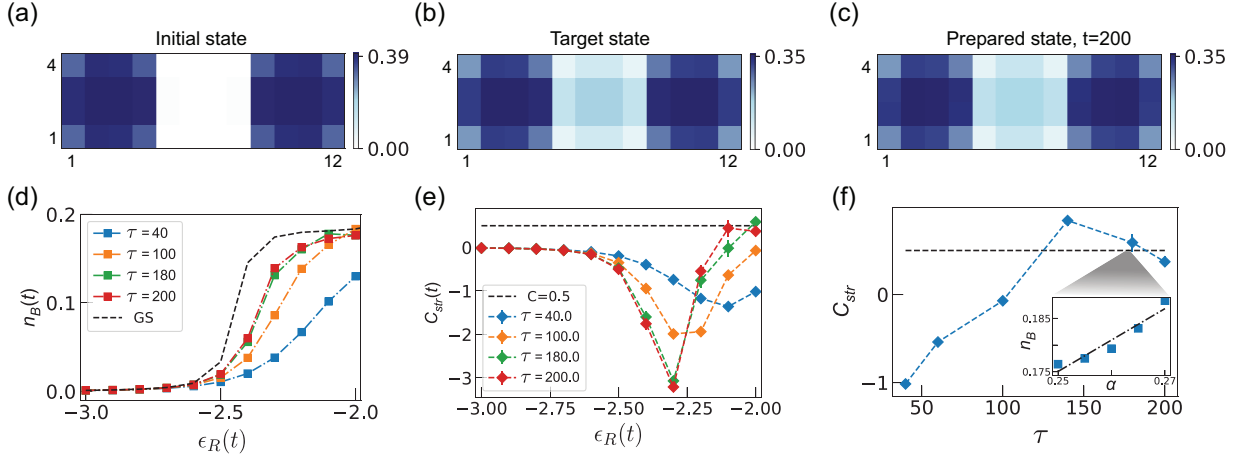

FIG. S5. **Preparing a fractional Chern insulator by using a linear ramp.** The spatial density distribution of (a) the initial state at $\epsilon_R = -3$, (b) the target state at $\epsilon_R = -2$ and (c) the prepared state at time $t = \tau = 200$. (d) The bulk density as a function of ϵ_R for different τ. The black dashed line corresponds to the adiabatic limit. (e) The local Středa marker $C_{str}(t)$ as a function of $\epsilon_R(t)$ for different τ. (f) The final Středa marker as a function of τ. Inset: linear fit of the density versus flux at $\tau = 180$, which gives $C_{str} \approx 0.59$. Here, we consider $N = 12$ hard-core bosons, and the system of size 4×4 is coupled with two reservoirs with $J_R = 0.15$, each of which has size 4×4. The error bars denote the standard error of a regression slope.

We start from a trivial state with 6 hard-core bosons in each reservoir, as shown in Fig. S5(a), leaving the system empty. After linearly ramping up the reservoir potential $\epsilon_R(t)$ from -3 until -2 within a duration τ, we track the bulk density, as evaluated within the central 2×2 sites, as a function of $\epsilon_R(t)$; see Fig. S5(d). Using numerical simulations based on density matrix renormalization group (DMRG) methods [85–89], one observes that the bulk density approaches the adiabatic-limit prediction for a sufficiently long ramping time. The sudden increase of the bulk density indicates a transition. As further confirmed by the local Středa marker in Fig. S5(e), the obvious dip (breakdown) of C_{str} indicates a change in the topological properties. By using sufficiently long ramping times, C_{str} gets close to the expected value $1/2$. The final Středa marker as function of total ramping time is plotted in Fig. S5(f), with the inset showing that a ramping time $\tau = 180$ leads to the marker's value $C_{str} \approx 0.59$.

B. Finite size effects

After demonstrating the validity of our injection scheme for the preparation of a small FCI, we now analyze how the efficiency of this scheme scales with the size of the reservoir, as well as with the size of the target system. Focusing on the sub-box configuration introduced in Fig.3(a) of the main text, we consider a target system of size $L_S \times L_S$ coupled with two identical reservoirs of size $L_R \times L_S$, where L_S and L_R denote the lengths of the system and reservoir, respectively.

We first investigate the effects of the reservoir length L_R by fixing $L_S = 4$ and the total particle number $N = 12$. We calculate the many-body gap ΔE as a function of the reservoir energy ϵ_R, within the range $-3 \leq \epsilon_R \leq -2$, where a transition is known to occur (see Fig. 3 in the main text). From this, we extract the minimal many-body gap ΔE_M, which sets the time-scale for adiabatic state preparation. The resulting quantity ΔE_M is plotted as a function of L_R in Fig. S6(a). We find that for $L_R \geq 3$, the minimal gap ΔE_M linearly decreases with L_R. Besides, by fixing
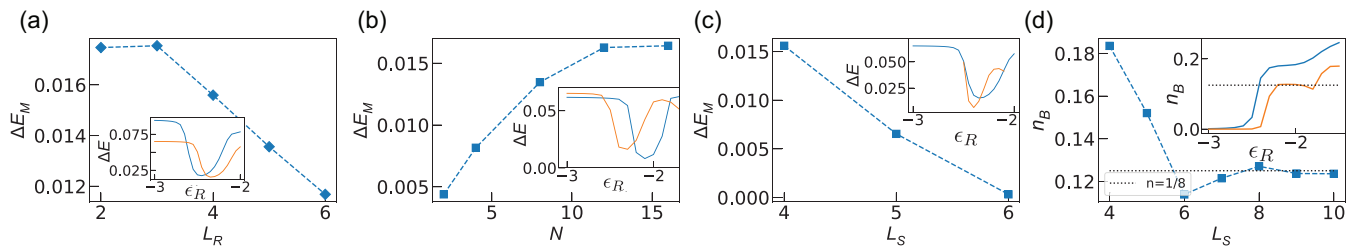
FIG. S6. **Finite size effects in the FCI-reservoir setup.** (a) The minimum gap ΔE_M as a function of the length of each reservoir L_R for a fixed total number of particles $N = 12$. Inset: The many body gap ΔE as a function of ϵ_R for $L_R=3$ (blue) and 4 (orange). (b) The minimum gap ΔE_M as a function of particle number N for a fixed $L_R = 4$. Inset: ΔE as a function of ϵ_R for $N=4$ (blue) and 12 (orange). In (a,b) we fix the system length $L_S = 4$. (c) The minimum gap ΔE_M as a function of the system length L_S for fixed $L_R = 4, N = 12$. Inset: ΔE as a function of ϵ_R for $L_S=4$ (blue) and 5 (orange). (d) The bulk density n_B as a function of L_S at $\epsilon_R = -2$ for $L_R = 4, N = 12$. Inset: n_B as a function of ϵ_R for $L_S = 4$ (blue) and $L_S = 8$ (orange). The dotted line indicates the expected $n = 1/8$ in the thermodynamic limit. The bulk density is averaged over a disk of radius $r = 1$ at the center of the system. In (a-d), we choose the width of the whole setup to be $W = L_S$ and use $J_R = 0.15, \alpha = 1/4$. The dashed lines are the guide to the eye.

$L_S = L_R = 4$, we find a non-linear increase of ΔE_M as a function of the total particle number N; see Fig. S6(b). Since the value of the minimal gap ΔE_M determines the time scale for a possible adiabatic state preparation, the results presented here indicate that it is favorable to consider a reservoir of small size with many particles.

We now analyze how the size of the system L_S influences the efficiency of the scheme, by fixing the reservoir length $L_R = 4$ and the particle number $N = 12$. As shown in Fig. S6(c), the minimal gap decreases with L_S, which signals the potential difficulty of preparing an FCI in a substantially larger lattice system. This limitation could be circumvent by optimizing the reservoirs (see above), or possibly, by combining the injection scheme with the cleaning method described in the main text. Another route for improvement could be offered by a double layered system-reservoir configuration; in practice, this could also be realized using two different internal states of an atom for the system and reservoir, respectively.

Last but not least, we analyze the (ideal) particle density expected within the bulk of the system n_B as a function of the system size L_S, for a fixed reservoir energy $\epsilon_R = -2$; see Fig. S6(d). It is interesting to note that the particle density n_B already approaches its thermodynamic-limit value $n_B = \nu\alpha = 1/8$ (expected for a $\nu = 1/2$ Laughlin state) for a system size $L_S \gtrsim 8$. Specifically, we find $n_B \simeq 0.127$ and $n_B \simeq 0.124$ for $L_S = 8$ and $L_S = 10$, respectively.

V. STATE PREPARATION VIA REPEATED CLEANING

A. Rabi cycles

The aim of this Appendix is to estimate optimal parameters for the vacuum-cleaning scheme, by analyzing a simplified few-level model.

In Fig. 4(a) of the main text, we presented a sketch of a simplified 3-level toy model for our system-reservoir setup. Our aim is to gain more intuition on our repeated cleaning protocol by analyzing the Rabi oscillations that occur between these levels upon coupling them. To be specific, we introduce the Level-0, Level-1, and Level-R to denote our (target) lowest Chern band, the first excited band and the reservoir band, respectively. The corresponding characteristic energies are represented by E_0, E_1 and ϵ_R in Fig. 4(a). Level-0 and Level-1 have the same coupling strength J_R with Level-R.

Starting from the situation where both the lowest and the excited bands are fully occupied, we aim to activate a coupling that keeps the lowest band occupation essentially unaffected, while cleaning off the population in the excited bands as much as possible. Specifically, in terms of the 3-level toy model, we analyze the occupation in Level-0 when the transition from Level-1 to Level-R is maximal. Here, we treat the 3-level toy model as two independent two-level systems: one describing the coupling of the reservoir to Level-0 and the other describing the coupling of the reservoir to Level-1.

In a two-level quantum system, it is well-known that the Rabi formula describes the transition from one level to the other. Starting from a state initially occupying the first level (denoted by a), the transition probability to the
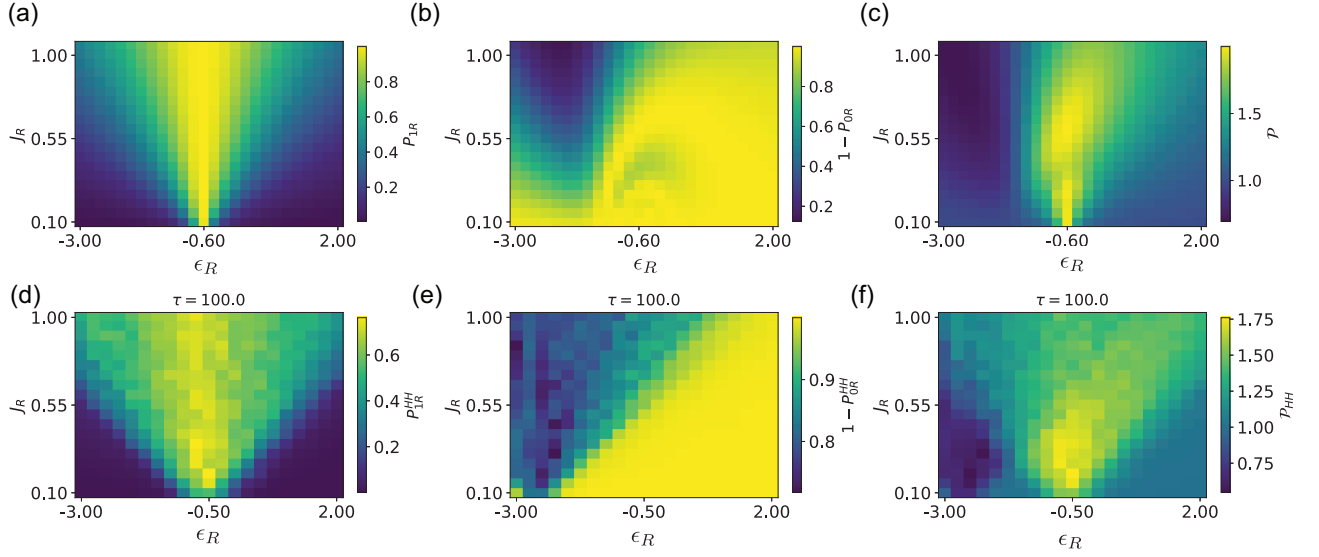
FIG. S7. **Rabi oscillations and quench dynamics.** (a) The maximal transition P_{1R}^{Max}, (b) the transition left in Level-0 $1 - P_{0R}$ at $t = t^*$, and the characteristic population $\mathcal{P}$ of the simplified 3-level toy model. (d) The excited band transition P_{1R}^{HH}, (e) the remaining lowest band population $1 - P_{0R}^{HH}$, and the characteristic population $\mathcal{P}_{HH}$ of the quench dynamics of our system-reservoir configuration at $t = 100$.

second level (denoted by b) reads

$$P_{ab}(t) = \frac{\gamma^2}{\gamma^2 + (E_a - E_b)^2/4} \sin^2\left(\sqrt{\frac{(E_a - E_b)^2}{4} + \gamma^2}\, t\right), \tag{S2}$$

where E_a, E_b represent the level energies and γ is the strength of coupling between these two levels.

We first analyze the transition from Level-1 to Level-R, and we establish its optimal regime by finding the maximal value $P_{1R}^{\mathrm{Max}} = P_{1R}(t^*)$ using Eq. S2; the time t^* will denote the optimal duration of the coupling. We plot P_{1R}^{Max} for different values of ϵ_R, J_R in Fig S7(a). When ϵ_R becomes resonant with $E_1 \simeq -0.6$, which is taken as the mean value of the excited Hofstadter band, the transition probability P_{1R} can take a value as large as 1. In order to study the remaining population in the Level-0 when P_{1R} is maximal, we plot $1 - P_{0R}$ at time $t = t^*$ in Fig S7(b).

Now, to identify an optimal regime for our control parameters, we define a figure of merit $\mathcal{P}$ as

$$\mathcal{P} = 1 - P_{0R} + P_{1R}. \tag{S3}$$

In the ideal case where the population in Level-1 is completely removed ($P_{1R} = 1$) while Level-0 remains perfectly unaffected ($P_{0R} = 0$), one has the maximal value $\mathcal{P} = 2$; vice versa one has the minimal value $\mathcal{P} = 0$. As shown in Fig. S7(c), it is preferable to set ϵ_R close to resonance with the excited band E_1 and to use a small coupling strength J_R, in order to empty the Level-1 while protecting the Level-0.

To make a further step towards our cleaning protocol, we now check the above-mentioned optimal parameter regime for a quench dynamics of our system-reservoir setup. Considering an initial state with $1/2$-filling per site within the HH system (the central sub-box), we investigate the quench dynamics by suddenly setting ϵ_R to a given value. Similarly, we now define the figure of merit $\mathcal{P}_{HH}$ for our HH system as,

$$\mathcal{P}_{HH} = 1 - P_{0R}^{HH} + P_{1R}^{HH}, \tag{S4}$$

where we can express the possibility of transition from band i to the reservoir in terms of the eigenstate populations ρ_j as

$$P_{iR}^{HH} = \sum_{j=1}^{N_i} (1 - \rho_j)/N_i, \tag{S5}$$

with $i = 0, 1$ and N_i being the number of bulk states belonging to band i. By plotting the figure of merit $\mathcal{P}_{HH}$ for different values of J_R, ϵ_R in Fig. S7(f), one identifies an optimal parameter regime, where ϵ_R is close to the mean
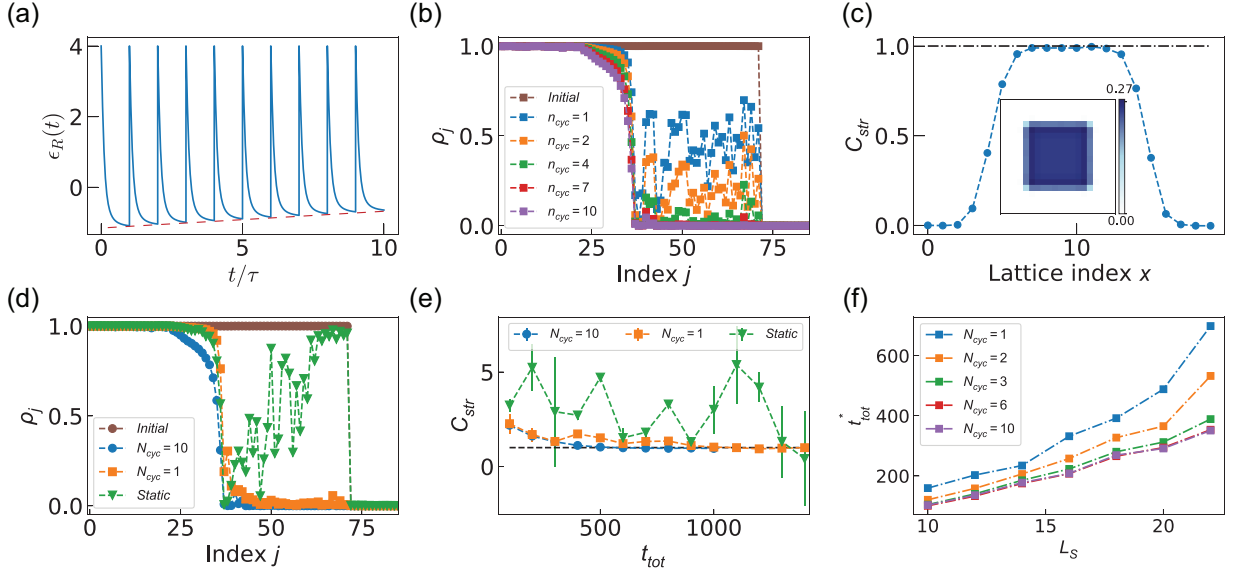
FIG. S8. **Preparing a Chern insulator based on cleaning.** (a) The repeated ramping protocol for ϵ_R according to a saturation function. The red dashed line is the guide to the eye. (b) Population in HH eigenstates for different n_{cyc} with $\tau = 60$ per cycle. (c) The local Středa marker of the evolved state with $n_{\text{cyc}} = 10, \tau = 60$ as a function of lattice indices along the middle row. Inset: the corresponding spatial density distribution of the evolved state. (d) Eigenstates population ρ_j as a function of state index j for the same total preparation time $t_{\text{tot}} = 500$. The blue dots represent our repeated cleaning protocol with a duration $\tau = 50$ per cycle; the orange squares corresponds to a single cleaning process (thus $\tau = 500$), and the green triangles are the results of using a static reservoir with $\epsilon_R \simeq -1.1$ (that is just below the excited band). (e) The local marker C_{str} as a function of the total preparation time t_{tot}. In the case of repeated cleaning, we use a duration $\tau = t_{\text{tot}}/N_{\text{cyc}}$ per cycle. The local marker is averaged over a disk at the center with a radius of $r = 3$. The error bars denote the standard error of a regression slope. (f) The typical time t_{tot}^* as a function of the system length L_S for different total cycle number N_{cyc}. During the scaling, we consider square boxes and keep the length ratio between the whole setup and the system as $L/L_S \simeq 1.6$. For (b-e), we partition a lattice of size 20×20 into a target 12×12 system (central box) and a surrounding reservoir with particle number $N = 72$. We set a flux $\phi = \pi/2$ in the system and $\phi = 0$ in the reservoir, and use $J_R = 0.15, \xi = 3$.

energy value E_1 of the excited band and where the coupling J_R is relatively weak. In contrast, when ϵ_R is set close to the mean energy of the lowest band $E_0 \simeq -2.7$, a small $\mathcal{P}_{HH}$ is found due to a heavy depletion of the lowest band. When ϵ_R is set to a very large value (off resonance), no transition takes place between the system and the reservoir, and thus $\mathcal{P}_{HH}$ saturates to 1. This analysis shows a qualitative agreement with the simplified Rabi model [Fig. S7(c)].

B. Dynamical cleaning scheme and scaling

Despite the identification of an optimal parameter regime (see above), a simple quench dynamics does not lead to a satisfactory preparation of the CI, i.e. a complete depletion of the excited bands while leaving the lowest band perfectly filled. This is essentially due to the finite dispersion of the HH bands. To solve this issue, we consider tuning ϵ_R in a time-dependent fashion, as we now explain.

We choose to dynamically tune the reservoir potential according to a saturation function,

$$\epsilon_R(t) = \epsilon_R^i - (\epsilon_R^i - \epsilon_R^f) t / (\sqrt{c\tau^2 + t^2}), \tag{S6}$$

with the initial value $\epsilon_R^i = 4$, a constant parameter $c = 0.02$ and the total ramping time τ. As shown in Fig. S8(a), after reaching the final value ϵ_R^f, we quickly lift ϵ_R to a high value. Since the system is now almost completely decoupled from the reservoir, one can easily remove the particles from the reservoir. The ability of preparing such an empty reservoir makes it possible to have several cycles. To increase the efficiency, one can design the final value of ϵ_R^f for each cycle n_{cyc} as

$$\epsilon_R^f(n_{\text{cyc}}) = \epsilon_R^f(1) + J_R \xi \frac{n_{\text{cyc}} - 1}{N_{\text{cyc}} - 1}, \tag{S7}$$

with $n_{\mathrm{cyc}} = 1, \cdots, N_{\mathrm{cyc}}$ and N_{cyc} is the total cycle number. The coefficient ξ controls the final value of ϵ_R. For the very first cycle, we take $\epsilon_R^f(1) = -1.1$ which is located right below the excited band.

Considering a many-body state at 1/2-filling as our initial state, we now apply our repeated cleaning protocol to prepare a CI in the system: we aim at removing the higher band populations but leaving the lowest Chern band almost perfectly filled. As shown in Fig. S8(b), we find an efficient depletion of the excited bands with the increase of the cycle number. During the ramp, the bulk states of the lowest band remain almost perfectly filled. This already points towards the realization of a CI state in the system. To further confirm its topological nature, we plot the local Středa marker (averaged over the surrounding 4 sites) for $n_{\mathrm{cyc}} = 10$ with $\tau = 60$ per cycle in Fig. S8(c), which shows a uniform bulk with $C_{\mathrm{str}} \approx 1$.

To demonstrate the advantages of using repeated cycles, we now compare the cleaning efficiency for three different situations: (i) an evaporative-type method using a static reservoir; (ii) a single but very long cleaning process (i.e. a "slowly-falling" elevator); (iii) our repeated cleaning scheme ("vacuum cleaner"). The results are shown in Fig. S8(d): Using a static reservoir only allows to get rid of a limited portion of excitations; see the green triangles in Fig. S8(d). In contrast, our repeated-cleaning protocol provides an efficient way to remove all excitations; see blue dots in Fig. S8(d). Importantly, increasing the number of cycles is shown to improve the cleaning (state-preparation) performance. Figure S8(e) further demonstrates the efficiency of the repeated-cleaning scheme, by showing the obtained Chern marker as a function of the total cleaning time: a Chern insulator cannot be prepared by using the static-reservoir scheme over realistic times.

Besides, in order to appreciate the scaling behavior, we plot a typical time t_{tot}^* corresponding to the uniformity $u = 1 - \sqrt{\sum_\ell (n_\ell - \alpha)^2 / N_\ell}$ above 0.96 in Fig. S8(f), where the uniformity is evaluated in a central disk of radius $r = 4$ containing N_ℓ sites. We find that the typical time increases more slowly with the system size as one increases the total number of cycles.

C. Full preparation protocol using the cleaning scheme

In the main text, we apply our repeated cleaning protocol to a realistic state, which has been prepared starting from a trivial metal (i.e. starting from a band structure with zero Chern numbers). Here we give more details about the full ramping protocol.

We start from a trivial metal in the presence of a large staggered potential, $\delta_\ell = [(-1)^m + (-1)^n]\delta/2$, with (m, n) being the lattice indices along x and y direction, respectively. We then linearly ramp up the flux in the lattice from 0 to the value of $\pi/2$. Since the system is still within a trivial regime (guaranteed by the large staggered potentials $\delta = 10$), one can ramp up the flux rather quickly. After that, we slowly reduce the staggered potential in order to change the topological nature of the bands; this transition generates excitations in the higher bands for a realistic quasi-adiabatic ramp; see the sequence in Fig. S9(a). The density distribution of the evolved state, across the topological phase transition, is shown in Fig. S9(b)-(d); this latter situation corresponds to the blue dots in the band populations shown in Fig. 4(b) in the main text.

With this realistic (but highly excited) state in hand, we now apply our repeated cleaning protocol. In order to progressively address the higher bands at each cycle, we set $\epsilon_R^f(1) = -1.14$ and $\xi = 14$ for the final value of ϵ_R^f defined in Eq. (S7); see also Fig. S9(a). In this case, the final value of ϵ_R^f in the last cycle reads 0.94, which is located near the top of the excited band. Note that even though we only consider a linear increase of ϵ_R^f at each cycle (for simplicity), a more efficient protocol could be designed by fine tuning ϵ_R^f within each cycle, e.g. by means of optimal control or even machine learning.
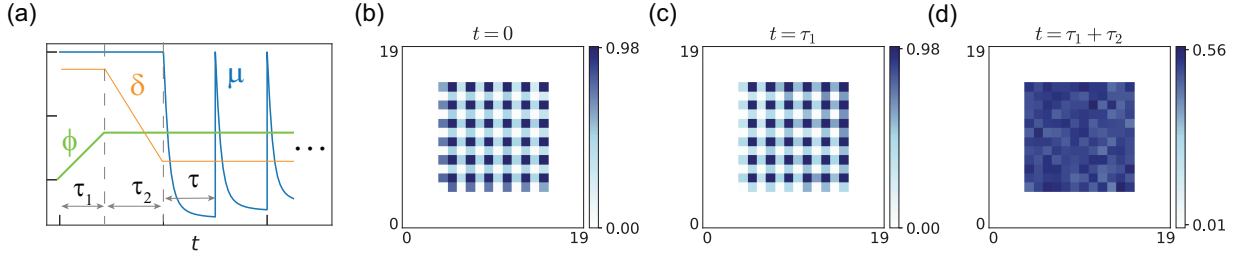
FIG. S9. **Full protocol for preparing CI based on cleaning.** (a) The full protocol for ramping system parameters. The flux is linearly increased from 0 to $\pi/2$ within τ_1, and then we decrease the staggered potentials δ from 20 to 0 within τ_2. After that, we apply our cleaning protocol cycle by cycle with τ being the ramping time per cycle. (b-d) The spatial density distributions at $t = 0, \tau_1$ and $\tau_1 + \tau_2$, respectively. Here, we consider the durations $\tau_1 = 100$, $\tau_2 = 300$ to tune ϕ and δ, respectively.

VI. COMPARING PARTICLE INJECTION AND REPEATED-CLEANING METHODS

In this Section, we compare the two types of state-preparation protocols that are presented in this work: (i) the particle-injection method (in monolayer but also bilayer configurations), and (ii) the repeated-cleaning protocol.

First of all, we remark that the state-preparation scheme based on the injection of particles (from the reservoirs to the system) requires a proper coupling between the bulk of the system (where the target state is located) and the reservoirs. In the limit of a large system ($L \to \infty$), an arbitrarily long time will be required for particles to travel from the reservoir to the center of the system, as one would deduce from the small spatial overlap between the reservoir states and the system's bulk states that are located at the center of the system; see Fig. S4(f). This limitation can be circumvented by considering a bilayer configuration (i.e. two layers of an optical lattice or two internal states of an atom), in which one layer represents the system and the other represents the reservoir. We illustrate this strategy in Figs. S10(b)-(c), which compare the eigenstate populations obtained at the end of the state-preparation process for the bilayer and monolayer ('surrounding') configurations, respectively. These results clearly show that the bilayer configuration does not suffer from the existence of isolated bulk states in the limit of a large system size.

In any case, we find that the strongest limitation of this injection scheme is related to the adiabatic nature of the preparation process: increasing the system size leads to a decrease in the many-body gap that needs to be traversed during the preparation process. This limitation concerns both the monolayer and bilayer configurations, as we now illustrate in Fig. S10(a): the monolayer configuration (with a surrounding reservoir) and the bilayer configurations both show a similar scaling of the many-body gap with respect to the system size.

We note that the limitation discussed above, associated with the adiabatic nature of the preparation process, would challenge any other approach relying on adiabaticity, such as adiabatic-quantum-state preparation starting from a trivial state and tuning various system parameters.

The repeated-cleaning protocol does not rely on adiabaticity, and in this sense, it is genuinely different from adiabatic-quantum-state preparation. To explicitly compare the particle-injection and repeated-cleaning schemes, we consider a system of size 20×20, which is partitioned into a target system of size 12×12 and a surrounding reservoir. According to Fig. S10(d), a total cleaning time $t_{\text{tot}} \approx 500$ would be sufficient to prepare a Chern insulator using the repeated-cleaning scheme. In contrast, applying the injection scheme to the same setting does not lead to a clean Chern-insulator state over this same preparation time $t_{\text{tot}} \approx 500$; see Fig. S10(c).
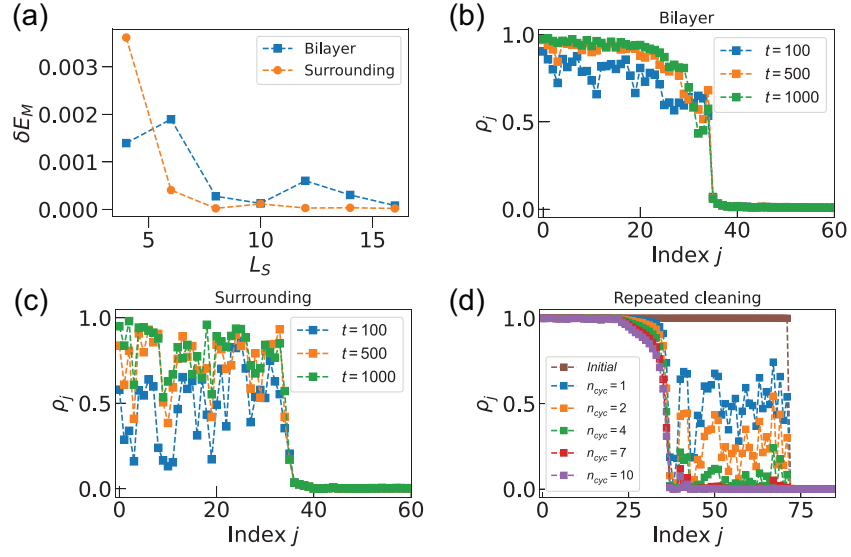
FIG. S10. (a) The minimal energy splitting δE_M as a function of the system length L_S. The blue squares represent a bilayer setup, and the orange dots describe a monolayer configuration as shown in Fig. S2(b). (b) The population of the eigenstates of the Hofstadter model in a bilayer setup. The trivial layer with vanishing flux is regarded as a reservoir, and the second layer described by the Hofstadter model represents the system. Here we consider a target system of size 12×12 with flux $\phi = \pi/2$ per plaquette. (c) The population of the eigenstates of the Hofstadter model in monolayer with a surrounding geometry. In both (b) and (c) we ramp up ϵ_R from -4.0 until -2.5 by using a saturation function with time t. (d) The HH eigenstate population by using the repeated-cleaning scheme with a duration $\tau = 50$ per cycle and $N_{\text{cyc}} = 10$ cycles in total; n_{cyc} denotes the cycle index. A total cleaning time of $t_{\text{tot}} = 500$ is found to result in a satisfactory preparation of the Chern-insulator state. Here the system is made of a 20×20 lattice, partitioned into a target system of size 12×12 and a reservoir. We set the hopping parameter $J_R = 0.2$ within the reservoirs and the connecting interface.